Refined Solution Structure of the LpxC−TU-514 Complex and pK_a Analysis of an Active Site Histidine: Insights into the Mechanism and Inhibitor Design[†,‡]

Brian E. Coggins,[§,‖] Amanda L. McClerren,[§,‖] Ling Jiang,[§] Xuechen Li,[⊥,@] Johannes Rudolph,[§] Ole Hindsgaul,[⊥,+]
Christian R. H. Raetz,[§] and Pei Zhou*,[§]

*Department of Biochemistry, Duke University Medical Center, P.O. Box 3711, 242 Nanaline Duke Building,
Research Drive, Durham, North Carolina 27710, and Department of Chemistry, University of Alberta,
W5-15 Edmonton, Alberta, Canada T6G 2G2*

Received October 10, 2004; Revised Manuscript Received November 11, 2004

ABSTRACT: Lipopolysaccharide, the major constituent of the outer monolayer of the outer membrane of Gram-negative bacteria, is anchored into the membrane through the hydrophobic moiety lipid A, a hexaacylated disaccharide. The zinc-dependent metalloamidase UDP-3-*O*-acyl-*N*-acetylglucosamine deacetylase (LpxC) catalyzes the second and committed step in the biosynthesis of lipid A. LpxC shows no homology to mammalian metalloamidases and is essential for cell viability, making it an important target for the development of novel antibacterial compounds. Recent NMR and X-ray studies of the LpxC from *Aquifex aeolicus* have provided the first structural information about this family of proteins. Insight into the catalytic mechanism and the design of effective inhibitors could be facilitated by more detailed structural and biochemical studies that define substrate−protein interactions and the roles of specific residues in the active site. Here, we report the synthesis of the ^{13}C-labeled substrate-analogue inhibitor TU-514, and the subsequent refinement of the solution structure of the *A. aeolicus* LpxC−TU-514 complex using residual dipolar couplings. We also reevaluate the catalytic role of an active site histidine, H253, on the basis of both its pK_a as determined by NMR titration and pH-dependent kinetic analyses. These results provide a structural basis for the design of more potent LpxC inhibitors than those that are currently available.

UDP-3-*O*-acyl-*N*-acetylglucosamine deacetylase (LpxC)[1] is an essential enzyme in Gram-negative bacteria, and is responsible for carrying out the committed step in the biosynthesis of lipid A (*1*). The hexaacylated disaccharide lipid A, also known as endotoxin, is the hydrophobic anchor of lipopolysaccharide, the primary component of the outer monolayer of the outer membrane of Gram-negative bacteria, and an essential protective barrier against such agents as detergents and antibiotics. LpxC recognizes and deacetylates monoacylated UDP-*N*-acetylglucosamine using a Zn^{2+} ion as a cofactor (*2*). The LpxC sequence contains a novel

HKXXD zinc-binding motif that is not found in other zinc metalloamidases (*3, 4*). As with many other zinc enzymes, addition of zinc to LpxC beyond 1:1 stoichiometry is inhibitory, implying that LpxC has an inhibitory zinc-binding site (*5*).

LpxC does not show sequence homology to any other family of enzymes. In most Gram-negative bacteria, LpxC is absolutely required for cell viability, making it an excellent target for the development of novel antibiotics to treat Gram-negative infections. LpxC inhibitors with antibacterial properties have been reported (*6, 7*). The most potent inhibitors of LpxC discovered to date—a group of phenyloxazoline hydroxamates with hydrophobic substituents—are effective at submicromolar concentrations against *Escherichia coli* LpxC (EcLpxC), with antibacterial efficacy comparable to that of the commercially available antibiotic ampicillin. However, the activity of these compounds varies greatly against LpxCs from different Gram-negative species, most likely as a result of structural differences between the LpxC enzymes (*6*). It is clear that the structural characterization of LpxCs from different organisms will be important for the understanding of inhibitor specificity and the development of more potent antibiotics.

Recently, both the solution and the crystal structures of an LpxC enzyme—that of the hyperthermophilic organism *Aquifex aeolicus* (AaLpxC)—were reported, providing the first structural information about this family of proteins (*3, 4*). The solution structure of this 32 kDa protein in complex

* To whom correspondence should be addressed. E-mail: peizhou@biochem.duke.edu. Phone: (919) 668-6409. Fax: (919) 684-8885.
§ Duke University Medical Center.
‖ These authors contributed equally to this work.
⊥ University of Alberta.
@ Current address: Department of Chemistry and Chemical Biology, Harvard University, 12 Oxford St., Cambridge, MA 02138.
+ Current address: Carlsberg Laboratory, DK-2500 Valby, Denmark.
1 Abbreviations: LpxC, UDP-3-*O*-acyl-*N*-acetylglucosamine deacetylase; AaLpxC, *Aquifex aeolicus* LpxC; EcLpxC, *Escherichia coli* LpxC; TU-514, 1,5-anhydro-2-*C*-(carboxymethyl-*N*-hydroxyamide)-2-deoxy-3-*O*-myristoyl-D-glucitol; NMR, nuclear magnetic resonance.

with a substrate-analogue inhibitor was determined at 50 °C using nuclear magnetic resonance (NMR) spectroscopy (*3*). This compound, known as TU-514 (1,5-anhydro-2-*C*-(carboxymethyl-*N*-hydroxyamide)-2-deoxy-3-*O*-myristoyl-D-glucitol), differs from the LpxC substrate in that it lacks the UDP moiety, its myristoyl ester chain does not contain a 3-hydroxy group, and its *N*-acetyl group is replaced with a methylhydroxamic acid, designed to chelate the catalytic zinc ion at the active site while presenting a nonhydrolyzable bond to the catalytic machinery. The crystal structure was determined by Whittington et al. at 2.0 Å resolution using a recombinant LpxC with its C-terminal 11 residues truncated, and with a C181A mutation (*4*). The protein was crystallized in the presence of 0.5 mM ZnSO$_4$, which provided enough zinc to saturate three specific binding sites in each monomer, and an additional site located between two monomers in the crystallographic asymmetric unit. Surprisingly, it was found that a fatty acid, interpreted as myristate (C$_{14}$), cocrystallized with the protein at the active site. The origin of the myristate chain present in the crystal structure is unknown.

These structural studies revealed that LpxC has a novel overall fold, a four-layer α/β sandwich, formed from two topologically similar domains. Each domain has its own unique insert segment, and the two inserts come together at one end of the sandwich to form the active site pocket. Both structures confirmed that the HKXXD sequence, which is conserved throughout the LpxC family and which was shown by mutagenesis to be required for catalysis, does indeed constitute a novel zinc-binding motif (*3, 5*). In addition, these studies revealed a highly unusual and intriguing feature of LpxC: A topologically closed loop of secondary structure in one of the domain inserts forms a hydrophobic passage into which the acyl chain of the inhibitor binds. In the solution structure, the inhibitor's acyl chain was found in this passage with the hexose ring bound inside the active site cavity. The X-ray structure showed a fatty acid bound in the same passage, with the carboxylate headgroup chelated to a second active site Zn^{2+}, presumed to be the inhibitory one. Data were also presented alongside the NMR structure showing that portions of the active site, including residues comprising the hydrophobic passage, experience significant dynamics in the absence of a ligand. Thus, it appears that a portion of LpxC either is in chemical exchange between ordered states or is disordered until an acyl chain is recognized.

Several models have been proposed to account for the mechanism of LpxC catalysis (*3–5*). Early studies of an E73A mutation revealed a loss of inhibition by excess zinc. On the basis of analogy with existing metalloamidases for which the catalytic general base is usually found to be a ligand for the inhibitory zinc ion, E73 was proposed to be a general base (*5*). Consistent with this hypothesis, later structural studies showed that this glutamate is indeed present in the active site and coordinates with the inhibitory zinc ion in the presence of high zinc concentrations (*4*). It was also postulated that a nearby histidine, H253, stabilizes the transition state. However, the initially reported high residual activity of the E73A mutant (∼10%) compared to wild-type LpxC raised concerns about the role of E73 as the general base (*3, 5*). This led to the proposal of an alternative mechanism in which H253 serves as a general base, and a nearby, absolutely conserved lysine, K227, stabilizes the

transition state (*3*). Mutations of H253 to either alanine or glutamine have less than 1% residual activity, emphasizing the significance of this residue in LpxC catalysis (*3, 5*).

A high-resolution structure of LpxC with a transition-state analogue would provide much insight into the detailed reaction mechanism of the enzyme. Unfortunately, the crystal structure of AaLpxC was determined with a bound fatty acid, and is thus less informative about the reaction mechanism. Although we have previously reported a solution structure of AaLpxC in complex with a substrate analogue at medium resolution, the interface between TU-514 and AaLpxC was not well defined. This was due to the limited number of intermolecular NOEs arising from relatively insensitive isotope-filtered experiments. Recently, the application of residual dipolar couplings to the refinement of solution structures has been shown to improve the quality and accuracy of NMR structures significantly (for reviews, see refs *8–11*). To gain better structural insight into the details of substrate binding and LpxC catalysis, we report here a high-resolution solution structure of AaLpxC, refined by residual dipolar couplings. The interactions of the substrate analogue inhibitor TU-514 with AaLpxC are now more clearly defined. In addition, we reevaluate the catalytic role of the active site residue H253 by determining its pK_a using NMR titration, and by comparing this value to the pH-dependent ionizations measured through kinetic studies for wild-type AaLpxC and an AaLpxC mutant. The refined solution structure and the charge state of the active site provide structural insights that might facilitate the design of novel LpxC inhibitors.

MATERIALS AND METHODS

Synthesis of Isotopically Enriched TU-514. TU-514 with a ^{13}C-labeled hexose ring (referred to as ^{13}C-labeled TU-514 in the following text) was synthesized starting from 99.9% uniformly ^{13}C-labeled D-glucose (Cambridge Isotope Laboratories, Andover, MA), which was converted into [U-^{13}C]-D-glucal in four steps (*12*). The D-glucal was processed to the final compound TU-514 following the synthetic route established by Li et al. (*13*) with minor modifications. Those were (1) the two-step oxidation of ozonizing alkene to aldehyde, followed by NaClO$_2$ oxidation to the carboxylic acid derivative, rather than the one-step oxidation using ruthenium tetroxide, and (2) amide formation using PyBOP/*i*-Pr$_2$EtN instead of EDC/Et$_3$N, both of which gave significantly cleaner reactions. The ^{13}C-labeled TU-514 was obtained in 18 steps from [^{13}C]-D-glucose with an overall yield of 7%. The electrospray ionization mass spectrum showed [M + Na$^+$] at *m/z* 460.2983 for this labeled compound (compared to *m/z* 454.2780 for the unlabeled compound). The detailed synthetic steps are provided as Supporting Information (Figure S1).

Isotope Labeling and Purification of AaLpxC. A pET21a plasmid encoding wild-type AaLpxC (*7*) was transformed into BL21(DE3) STAR cells (Invitrogen, Carlsbad, CA). ^{15}N- and ^{15}N/^{13}C-labeled AaLxpC were expressed by growing cells in M9 minimal media using either [^{15}N]NH$_4$Cl or [^{15}N]NH$_4$Cl and [^{13}C]glucose, respectively, as the sole nitrogen and carbon sources (Cambridge Isotope Laboratories, Andover, MA). Perdeuterated, uniformly ^{15}N/^{13}C-labeled AaLpxC was expressed by growing cells in D$_2$O and using

[^{15}N]NH$_4$Cl and deuterated [^{13}C]glucose as the nitrogen and carbon sources (Cambridge Isotope Laboratories). The cells were induced for 3−4 h at 20 °C and were then harvested by centrifugation at 4000 rpm for 30 min using a Beckman Coulter Avanti J-25 centrifuge. The induced cells were lysed in 25 mM HEPES, 300 mM KCl, pH 7.0, with 1 mM DTT by passing through a French pressure cell at 11 000 psi three times. After centrifugation at 21 000 rpm for 30 min (Beckman Coulter Avanti J-25), the supernatant was loaded onto a Q-sepharose fast flow column (GE Healthcare, Piscataway, NJ) and was eluted with a linear salt gradient. The fractions containing AaLpxC were combined, concentrated to approximately 5 mL, and further purified by size-exclusion chromatography with a Sephacryl S-200 column (GE Healthcare).

Sample Preparation and NMR Spectroscopy. The purified recombinant protein was allowed to bind at equal molar ratio to either ^{13}C-labeled TU-514 or unlabeled TU-514 at 37 °C for 1 h, then concentrated, and exchanged into an NMR buffer containing 25 mM sodium phosphate, pH 6.5, 100 mM KCl, 2 mM DTT, 5% deuterated DMSO, and 5% D$_2$O. All NMR experiments were carried out on either a Varian INOVA 600 MHz spectrometer or a Varian INOVA 800 MHz spectrometer at 50 °C unless otherwise noted. For structural refinement of the AaLpxC−TU-514 complex, a 3D ^{13}C NOESY-HSQC experiment with a mixing time of 150 ms was carried out to determine the intermolecular NOEs between the hexose ring of TU-514 and AaLpxC.

Residual dipolar couplings were determined from the difference in the corresponding heteronuclear couplings measured in an isotropic medium (water) and in a liquid crystalline medium of Pf1 filament phage. Efforts to measure the residual dipolar couplings of AaLpxC in Pf1 phage in the original NMR buffer with low salt concentrations (100 mM KCl) were not successful, probably due to interactions between AaLpxC and Pf1 phage. As a result, the experiment was conducted in the presence of 500 mM KCl in Pf1 phage. Concentrated Pf1 filamentous phage (ASLA, Ltd., Riga, Latvia) was preequilibrated in the sample buffer by spinning at 80 000 rpm for 4 h in a Beckman Coulter Optima ultracentrifuge and by resuspending the phage pellet in the final sample buffer. This concentrated phage solution was added directly into the NMR samples. The final phage concentration was estimated to be 12−15 mg/mL on the basis of a 13.2 Hz residual quadrupolar splitting of the D$_2$O resonance. Two samples were used to determine the residual dipolar couplings of AaLpxC and TU-514. The majority of the HN residual dipolar couplings were determined via an HNCO-based experiment (*14*) using a perdeuterated, ^{15}N/^{13}C-labeled AaLpxC in complex with unlabeled TU-514. Due to the extreme thermal stability of AaLpxC, approximately 1/3 of the amide protons did not exchange with H$_2$O even after an extended incubation period (over a week at 50 °C); the residual dipolar couplings of these amides were determined in D$_2$O using a 2D ^{1}H−^{15}N IPAP experiment (*15*) with a sample containing ^{15}N-labeled AaLpxC in complex with ^{13}C-labeled TU-514. Residual dipolar couplings of TU-514 were determined with the same sample using a high-resolution ^{1}H−^{13}C HSQC experiment without proton decoupling during the ^{13}C evolution period. Errors in residual dipolar couplings were estimated on the basis of repeating the same measurement twice.

To investigate the binding of UMP or UDP to AaLpxC, UMP or UDP disodium salt (Sigma-Aldrich, St. Louis, MO) was dissolved in the NMR buffer with 5% deuterated DMSO to produce a 5 mM stock solution. A series of ^{1}H−^{15}N HSQC spectra of AaLpxC or the AaLpxC−TU-514 complex were collected in the presence of increasing molar ratios (from 1:3 to 3:1) of UMP or UDP. No chemical shift perturbation was observed for AaLpxC or the AaLpxC−TU-514 complex during the entire titration range.

Data Processing, Spectral Analysis, and Structure Calculation. All NMR data were processed using NMRPipe (*16*) and analyzed in XEASY (*17*). The residual dipolar couplings were extracted using the automatic peak picking routine PIPP (*18*). The scale of one-bond HC residual dipolar couplings between axial protons and the attached carbon atoms of the TU-514 hexose ring was normalized relative to that of HN (*19*).

By iterative structural refinement and analysis of the various NOESY spectra, we were able to identify 888 additional NOE constraints, 60% of which are long-range ($|i − j| \geq 5$) constraints. A statistical analysis of the complete set of NOE constraints revealed that a large portion of the long-range NOE distance constraints between domains I and II of LpxC were derived from methyl−methyl NOE experiments using a ^{15}N/^{13}C-labeled, VIL-methyl-protonated, otherwise deuterated AaLpxC−TU-514 sample. We had previously used only upper limit constraints (6 Å) for these methyl cross-peaks due to concerns about spin diffusion with the long mixing time (175 ms). Although this treatment causes minimal distortion for a single-domain protein due to the geometrical restraints, it may produce a much more loosely packed structure for multidomain proteins in which most of the interdomain NOEs are derived from such methyl−methyl cross-peaks. Since the methyl−methyl NOEs were measured using a highly deuterated protein except for the methyl groups of valine, leucine, and isoleucine residues, we suspected that the effect of spin diffusion may be smaller than that of a protonated sample, thus permitting the use of more accurate distance restraints. Supporting this hypothesis, analysis of the methyl−methyl NOEs with the same mixing time (175 ms) from perdeuterated, ^{15}N/^{13}C-labeled, VIL-methyl-protonated human carbonic anhydrase II showed a good correlation between the NOE-derived methyl distances and those measured in the crystal structure (data not shown). To utilize the methyl−methyl NOE information more efficiently, we have here divided the methyl−methyl cross-peaks into different classes (<3.50, <4.00, <4.50, <5.5, and <7.0 Å) according to the relative intensity ratios (>0.3, 0.2−0.3, 0.12−0.2, 0.02−0.12, and <0.02) of these long-range methyl−methyl cross-peaks with respect to intraresidue methyl−methyl cross-peaks that are fixed in distance. We were also able to identify 16 additional intermolecular NOEs between AaLxpC and the hexose ring of TU-514 via a ^{13}C-separated 3D NOESY-HSQC experiment using the ^{13}C-labeled TU-514. The structures were initially calculated without residual dipolar couplings. The alignment tensor was then estimated by fitting the measured residual dipolar couplings with the calculated NMR structures using the MODULE program (*20*). The axial components of the estimated alignment tensor were then used in the structural refinement using the XPLOR-NIH simulated annealing protocol (*21*). Twenty-five structures were calculated with

Table 1: Primers Used for the Construction of AaLpxC Mutants

mutation	primer sequence
H19N	5′ primer: agc ttt gag ggt gtc ggt ata **AAC** aca ggt gaa tac tca aaa tta
	3′ primer: taa ttt tga gta ttc acc tgt **GTT** tat acc gac acc ctc aaa gct
H29N	5′ primer: gaa tac tca aaa tta atc ata **AAT** ccc gaa aaa gaa gga aca gga
	3′ primer: tcc tgt tcc ttc ttt ttc ggg **ATT** tat gat taa ttt tga gta ttc
H50A	5′ primer: gga gtt tac ata ccc gca aga **GCG** gag ttc gtc gtt cac aca aat
	3′ primer: att tgt gtg aac gac gaa ctc **CGC** tct tgc ggg tat gta aac tcc
H55N	5′ primer: gca aga **GCG** gag ttc gtc gtt **AAC** aca aat cac tcc acg gat tta
	3′ primer: taa atc cgt gga gtg att tgt **GTT** aac gac gaa ctc **CGC** tct tgc
H58N	5′ primer: gag ttc gtc gtt **AAC** aca aat **AAC** tcc acg gat tta ggc ttt aaa
	3′ primer: ttt aaa gcc taa atc cgt gga **GTT** att tgt **GTT** aac gac gaa ctc
C181A	5′ primer: ata gtc ctt gcg cgg act ttt **GCG** ttt gac tgg gaa ata gaa cac
	3′ primer: gtg ttc tat ttc cca gtc aaa **CGC** aaa agt ccg cgc aag gac tat
H188Y	5′ primer: **GCG** ttt gac tgg gaa ata gaa **TAC** att aaa aaa gtc ggt ctt ggg
	3′ primer: ccc aag acc gac ttt ttt aat **GTA** ttc tat ttc cca gtc aaa **CGC**
H253N	5′ primer: ttt tac tcc ttc agg gga ggg **AAC** tcg ctc aac gta aaa ctc gta
	3′ primer: tac gag ttt tac gtt gag cga **GTT** ccc tcc cct gaa gga gta aaa
H275STOP	5′ primer: aaa ctt act cgt gat tta cct **TAA** ctt cct tcc gtc caa gct ctc
	3′ primer: gag agc ttg gac gga agg aag **TTA** agg taa atc acg agt aag ttt

a backbone RMSD of 0.42 Å and a heavy-atom RMSD of 1.11 Å. None of the reported structures show NOE violations >0.4 Å or dihedral angle restraint violations >4°.

Mutagenesis and Sample Preparation. The single-point mutant H253A of wild-type AaLpxC was reported previously, and was used to identify the resonance of H253 in wild-type AaLpxC (5). Additional point mutations of AaLpxC were constructed starting from a pET21a plasmid encoding the wild-type AaLpxC. A series of seven mutations, including six nonconserved histidines (H29N, H50A, H55N, H58N, H188Y, and H275stop) and a cysteine (C181A) were made using the Quikchange kit following the standard protocol (Stratagene, La Jolla, CA). This construct is referred as AaLpxC-mut7 in the following text. Additional constructs were made to include either H19N (AaLpxC-mut8) or H19N/H253N (AaLpxC-mut9) in addition to these mutations. The primer sequences used to make these constructs are listed in Table 1. Existence of the correct mutations was confirmed by DNA sequencing. Finally, these expression plasmids were transformed into BL21(DE3) STAR cells for the overexpression of unlabeled protein or BL21(DE3) his⁻ cells for the production of AaLpxC proteins with histidines specifically ^{13}C-labeled at the C2′-position (22). To ensure efficient labeling, these cells were initially grown in regular M9 minimal media supplemented with unlabeled histidine, until the OD_{600} reached 0.4. The cells were harvested by centrifugation at 4000 rpm using a Beckman Coulter centrifuge (Avanti J-25) for 30 min and resuspended in M9 minimal media, supplemented with C2′-^{13}C-labeled histidine as the sole histidine source. Our initial effort in obtaining histidine-labeled protein resulted in background labeling of aromatic residues, although the reason for such scrambling is not clear to us. To suppress this undesired background labeling, the induction time was kept short (3−4 h) and unlabeled aromatic residues (Tyr, Phe, and Trp) were also added to the solution immediately before induction to prevent background scrambling from histidine to other aromatic residues.

Histidine Titration. Phase-sensitive 2D ^{1}H−^{13}C Watergate-HSQC experiments were collected on a Varian INOVA 600 MHz spectrometer equipped with a cryoprobe. Water magnetization was flipped back to the +z axis before detection to avoid water saturation. Before each experiment, NMR samples were exchanged into the desired NMR buffer containing 20 mM phosphate (from pH 6.0 to pH 8.0) or 20 mM CHES (from pH 8.5 to pH 10.0), 100 mM KCl, and 5% D_2O. To maintain the solubility of AaLpxC at a broad pH range (from pH 6.0 to pH 10.0), the titration experiments were performed at 37 °C. ^{1}H and ^{13}C chemical shifts of the histidines were referenced to DSS (23). The ^{13}C chemical shifts of the C2′ atom of H253 in AaLpxC-mut7 at different pH values were fit to eq 1 to determine the pK_a.

$$\delta = \frac{\delta_1 + \delta_2(10^{pH-pK_a})}{1 + 10^{pH-pK_a}} \quad (1)$$

pH-Dependent LpxC Activity Assays. Assays of AaLpxC were performed with the substrate UDP-3-O-((R)-3-hydroxymyristoyl)-N-acetylglucosamine, prepared as previously described (2, 5, 7, 24). Both ^{32}P-labeled and nonradioactive carrier substrates were prepared. The specific activity of the radioactive substrate used varied from 200 000 to 5 000 000 cpm/nmol. Wild-type AaLpxC and the seven-residue mutant AaLpxC-mut7 were assayed in a three-component buffer system containing 100 mM sodium acetate, 50 mM bis-Tris, and 50 mM Tris across a pH range from 4.0 to 9.5. Parallel assays were performed in the buffers used for the NMR titration studies, which contained 20 mM sodium phosphate and 100 mM KCl or 20 mM CHES and 100 mM KCl across a pH range from 6.0 to 10.0. The pHs of the buffers were routinely checked under mock assay conditions at 37 °C and adjusted accordingly. All reaction mixtures contained 1 mg/mL BSA. Assays were performed at 37 °C in a heat block. For the V_{max} studies, assays were performed at a substrate concentration of 25 μM, 5-fold higher than the K_M of wild-type AaLpxC. For the k_{cat}/K_M studies, assays were performed at low substrate concentrations under which the rate of the reaction doubles at each 2-fold increase in substrate concentration (0.044−2 μM). Reaction samples (5 μL) were removed at specific time points and quenched with 1 μL of 1.25 M NaOH. Further incubation at 30 °C for 10 min fully deacylated both substrate and product, yielding ^{32}P-labeled UDP-glucosamine or UDP-N-acetylglucosamine. Addition of 1 μL of 1.25 M acetic acid neutralized the samples. BSA was precipitated by addition of 1 μL of 5% TCA, followed by incubation on ice for 5 min and centrifugation for 3 min. Samples were then spotted (1 μL) on PEI-cellulose TLC

plates (5 000−25 000 cpm/sample) which were developed in 0.2 M guanidine hydrochloride. The plates were exposed to imaging screens overnight and quantified using a PhosphorImager and ImageQuant software. All assays were performed in duplicate or quadruplicate, and product formation (<10% overall conversion) was linear over the time course of the assay.

Steady-state kinetic parameters k_{cat}/K_M and V_{max} (k_{cat} approximation) and standard errors for LpxC activity were determined by a fit of initial velocities to the Michaelis−Menten equation (*25*). The pH-dependent ionizations were determined by a fit of steady-state parameters to eq 2, where v is the observed rate of the reaction, C is the pH-independent rate, [H] is the concentration of hydrogen ions, and K_a and K_b reflect the ionization constants of the acid and base species, respectively (*26*).

$$v = \frac{C}{1 + [H]/K_a + K_b/[H]} \qquad (2)$$

Inhibition Assays of LpxC. Activity assays of LpxC were performed as described above. For the inhibition of LpxC by UMP, UDP, myristate, or laurate, the nucleotide or fatty acid was added to the reaction mixture containing the substrate. LpxC enzyme was added to start the reaction. The substrate concentration in the final assay mixture was 4 μM. Assays were performed in 25 mM sodium phosphate buffer, pH 7.4, at 30 °C and contained 1 mg/mL BSA. Nucleotides were dissolved in water, and fatty acids were dissolved in DMSO. The final DMSO concentration in the reactions containing fatty acids was 10%. The percentage of remaining activity for each reaction containing nucleotide or fatty acid was determined by normalizing the specific activity against the wild-type enzyme containing no nucleotide or fatty acid.

RESULTS

Description of the Refined Solution Structure. The refined structure of AaLpxC is noticeably more compact than the unrefined structure, particularly between the two domains. This is largely due to the use of scaled methyl−methyl NOE constraints rather than the upper limit constraints used previously. Incorporation of residual dipolar couplings significantly improved the precision of the backbone atoms in the refined solution structure. Compared to the previously reported structure (*3*), the backbone root-mean-square deviation (RMSD) from the average structure has decreased from 0.63 to 0.42 Å. However, the RMSD improvement in side chain heavy atoms is relatively minor (from 1.19 to 1.11 Å). A superposition of the final 25 calculated structures is shown in Figure 1a; the ribbon diagram is shown in Figure 1b. A summary of the structural statistics is shown in Table 2.

The overall topology of AaLpxC remains unchanged. It contains two domains, each with a layer of two helices packing against a layer of a five-stranded β-sheet. The protein is formed with helices located at the interior and the two β-sheets covering the outside. In addition to these main structural elements, each domain contains an insert region. These insert regions are positioned on top of the two domains and are oriented perpendicularly to the main β-sheet. The insert region of domain II also contains a hydrophobic

passage that encompasses the acyl chain of the TU-514 inhibitor (Figure 1c).

The largest changes upon refinement involve two loops in insert region II (residues 195−198 and 213−216). These two loops are now better defined and deviate from the conformation of 3_{10} helices reported previously (Figure 1d) (*3*). The inclusion of residual dipolar coupling data in the refinement also affected the position and orientation of strand 0 (β0) in domain I (residues 4−7), which is now positioned closer to the loop connecting helix 1 (α1) and strand 5 (β5) in domain I and is somewhat twisted (Figure 1e).

Comparing the backbone heavy atoms of the refined solution structure of the AaLpxC−TU514 complex to those of AaLpxC in the crystal structure (*4*) shows an RMSD of 0.85 Å.

Determination of Additional Interfacial NOEs and Orientation of the TU-514 Hexose Ring. Considerable effort has been devoted to the development of NMR pulse sequences that differentiate intermolecular NOEs from intramolecular NOEs (for reviews, see refs *27* and *28*). The common feature of such experiments is the inclusion of additional INEPT steps that allow the selection or elimination of a specific subset of signals. For large protein complexes, transverse relaxation caused by these additional delays usually leads to significant signal loss of the intermolecular NOEs. In addition, the nonuniform distribution of proton−carbon heteronuclear couplings in proteins may cause incomplete suppression of intramolecular NOEs and introduce artifacts. Previously, we determined the intermolecular NOEs using an [F1] ^{13}C-filtered/[F2] ^{13}C-separated 3D NOESY-HSQC experiment (*29*). The availability of the refined solution structure and the crystal structure allowed us to cross-examine existing intermolecular NOEs and identify more intermolecular NOEs from this experiment. Among these additional NOEs, we were able to identify a cross-peak between the terminal methyl of the acyl chain of TU-514 and the Hγ2 methyl group of V205. Since the Hγ1 methyl of V205 shows a chemical shift (0.61 ± 0.04 ppm) similar to that of the terminal methyl group of the TU-514 acyl chain (0.64 ± 0.04 ppm), this cross-peak was previously deemed an artifact caused by the incomplete suppression of Hγ1 methyl within the same residue and was not assigned. Inclusion of these additional intermolecular NOEs created a curvature (~70−90°) for the terminal methyl and the last two methylene groups of the acyl chain of TU-514. It is interesting to note that, in the refined solution structure, the terminal methyl of the C14 acyl chain of TU-514 is positioned among three hydrophobic residues (Y212, V205, and L200) and shows strong intermolecular NOEs to all three residues (*3*). The addition of a methylene group past this length (14 carbons) would mostly likely introduce van der Waals clashes and lead to decreased binding affinity. As a result, LpxC might not recognize acylated UDP-*N*-acetylglucosamines containing more than 14 carbons efficiently.

Although the conformation of the TU-514 acyl chain and the shape of the hydrophobic passage had become well defined, we were still only able to detect a few NOEs to the hexose ring of TU-514. To overcome this problem, we resorted to a labeling strategy to identify intermolecular NOEs with a nonfiltered experiment (*30*−*33*). This approach has yielded improved sensitivity and better suppression of spectral artifacts. We modified a synthetic strategy reported
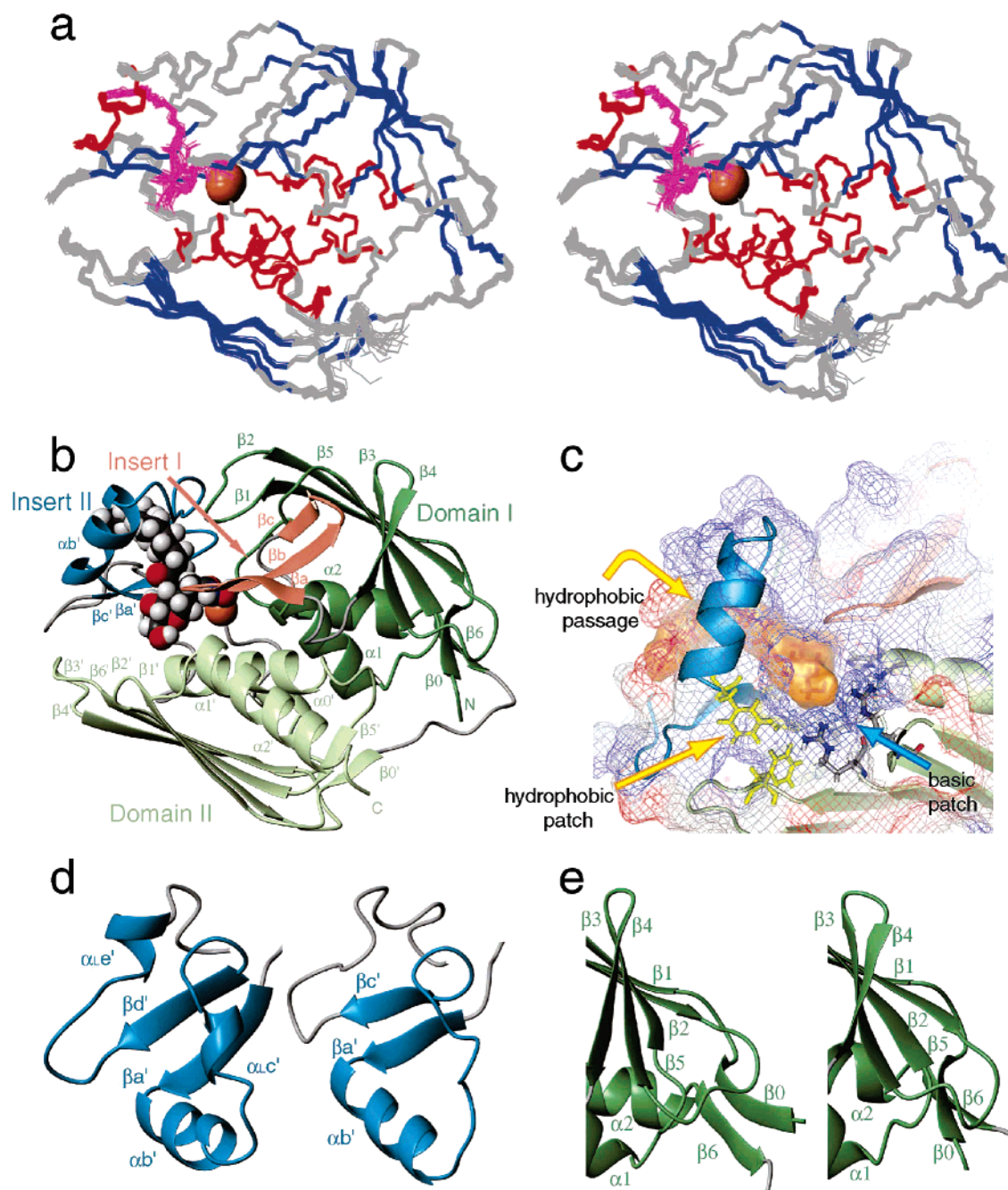
FIGURE 1: Refined solution structure of the AaLpxC−TU514 complex. (a) Stereoview of 25 calculated structures with β-stands colored in blue, α-helices in red, TU-514 in purple, and Zn^{2+} in coral. (b) Ribbon diagram of the AaLpxC−TU514 complex. Domain I is colored in dark green, domain II in pale green, insert I in coral, and insert II in blue. TU-514 is displayed as a ball-and-stick model. The secondary structure is labeled. (c) Environment of the active site showing the hydrophobic passage and the additional hydrophobic and positively charged basic surface patches that may contribute to the binding affinity of designed inhibitors. The secondary structure is colored as in panel b. Residues that form a hydrophobic patch are colored in yellow, residues forming a basic patch are colored in the CPK color scheme, and TU-514 is colored in purple. The surface of TU-514 is colored in orange to show its interaction within the hydrophobic passage. The electrostatic potential calculated by GRASP (*51*) is superimposed onto the mesh surface of the protein. (d, e) Ribbon diagrams illustrating the difference of insert II of domain II (d) and β0 (e) of domain I before (left) and after (right) refinement. The secondary structure is labeled and colored as in (b). Panels a, b, d, and e were prepared with MOLMOL (*52*). Panel c was prepared with PyMOL (DeLano Scientific).

by Li et al. (*13*), starting from [^{13}C]glucose, to incorporate ^{13}C into all six carbon atoms of the hexose ring of TU-514. Thus, we are able to detect intermolecular NOEs to the hexose ring directly using a ^{13}C-separated 3D NOESY-HSQC experiment. The intermolecular NOEs can be identified by excluding the signals from TU-514 (Figure 2a). This approach has led to the identification of 11 additional intermolecular NOEs to the hexose ring, vastly improving the

accuracy of the interface between the hexose ring of TU-514 and AaLpxC. To determine the precise orientation of the hexose ring, we have measured the one-bond ^{1}H−^{13}C residual dipolar couplings of TU-514 in an isotropic medium and in Pf1 phage. The measured ^{1}H−^{13}C residual dipolar couplings were normalized against the ^{1}H−^{15}N residual dipolar couplings measured for AaLpxC under the same conditions. The NOE patterns of TU-514 are consistent with

Table 2: Structural Statistics for the LpxC−TU-514 Complex (25 Structures)[a]

protein (LpxC)		ligand (TU-514)	
no. of NOE distance restraints	4502	no. of NOE distance constraints	29
intraresidue	1713	no. of dihedral angle constraints[f]	6
sequential ($|i − j| = 1$)	827	no. of residual dipolar couplings[g]	4
medium-range ($|i − j| \leq 4$)	423	protein−ligand interface	
i, i + 2	145	no. of NOE distance constraints	48
i, i + 3	204	deviations from idealized geometry	
i, i + 4	74	bonds (Å)	0.00166 ± 0.00004
long-range ($|i − j| \geq 5$)	1309	angles (deg)	0.378 ± 0.010
hydrogen bonds[b]	230	impropers (deg)	0.316 ± 0.005
no. of dihedral angle constraints[c]	745	average RMSD to the mean structure	
no. of residual dipolar couplings	189	backbone (residues 3−268) (Å)	0.42
dipolar coupling R factor of $^1D_{NH}$ (%)[d]	3.6 ± 0.1	heavy atoms (residue 3−268) (Å)	1.11
Ramachandran plot[e]			
favored region (98%) (%)	94.42		
allowed region (>99.8%) (%)	99.94		

[a] None of these structures exhibit distance violations greater than 0.4 Å or dihedral angle violations greater than 4°. [b] Two constraints per hydrogen bond ($d_{HN−O} \leq 2.0$ Å and $d_{N−O} \leq 3.0$ Å) are implemented for amide protons protected from solvent exchange. [c] Dihedral angle constraints were generated by TALOS on the basis of backbone atom chemical shifts and by the HABAS module in DYANA on the basis of NOE constraints (46, 47). [d] The R factor for residual dipolar coupling is defined as the ratio of the RMS deviation between observed and calculated values to the expected RMS deviation if the vectors were randomly distributed (48). [e] MOLPROBITY was used to assess the quality of the structures (49, 50). [f] Six dihedral angle constraints were used to maintain the chair conformation of the hexose ring of TU-514, which is consistent with the NOE patterns observed. [g] The average value of the residual dipolar couplings of the four parallel axial H−C bonds at positions 2−5 on the hexose ring of TU-514 is used for the calculation.
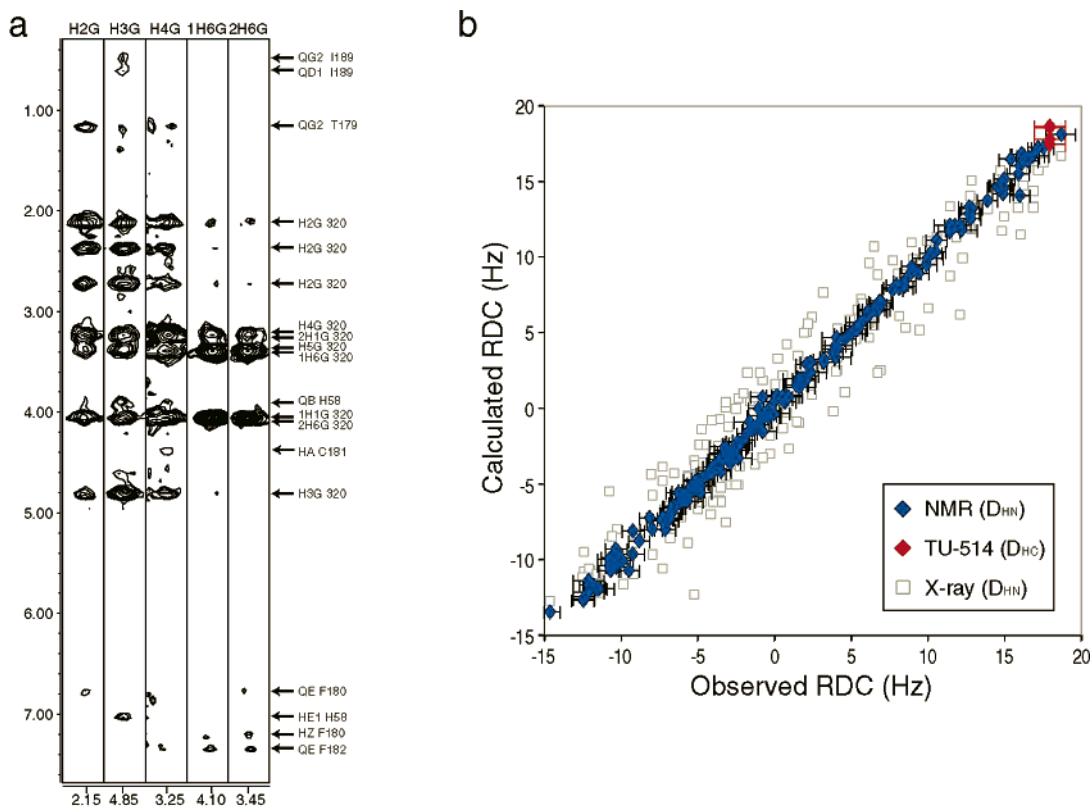
FIGURE 2: (a) Sample strips of the ^{13}C NOESY-HSQC spectrum using a ^{13}C-labeled TU-514. Intramolecular cross-peaks to TU-514 (labeled as residue 320, with atom nomenclature as described previously (3)) and intermolecular cross-peaks to AaLpxC are labeled. (b) Correlation between observed and calculated $^1D_{NH}$ for the refined solution structure (filled) and the crystal structure (open) and $^1D_{CH}$ for TU-514 (red).

a chair conformation of the hexose ring. In such a conformation, all the axial H−C bonds are parallel and thus should possess the same residual dipolar couplings. As a result, only the average value of the measured $^1H−^{13}C$ coupling was used for these bonds during the structure calculation. The agreement between measured and predicted residual dipolar couplings of the axial H−C bonds from the hexose ring of TU-514 and the backbone H−N bonds from AaLpxC in the refined solution structures is shown in Figure 2b. In the

refined solution structure, the hexose ring of TU-514 is packed more closely to the β-strand (βa′) of insert II and is oriented parallel instead of perpendicular to strand βa′ of insert II.

Determination of the Protonation State of H253 in Wild-Type AaLpxC. In a parallel study, we have recently shown that the deacetylation of UDP-3-O-acyl-N-acetylglucosamine by wild-type AaLpxC at 50 °C is dependent on two ionizations and displays a bell-shaped pH profile for catalytic
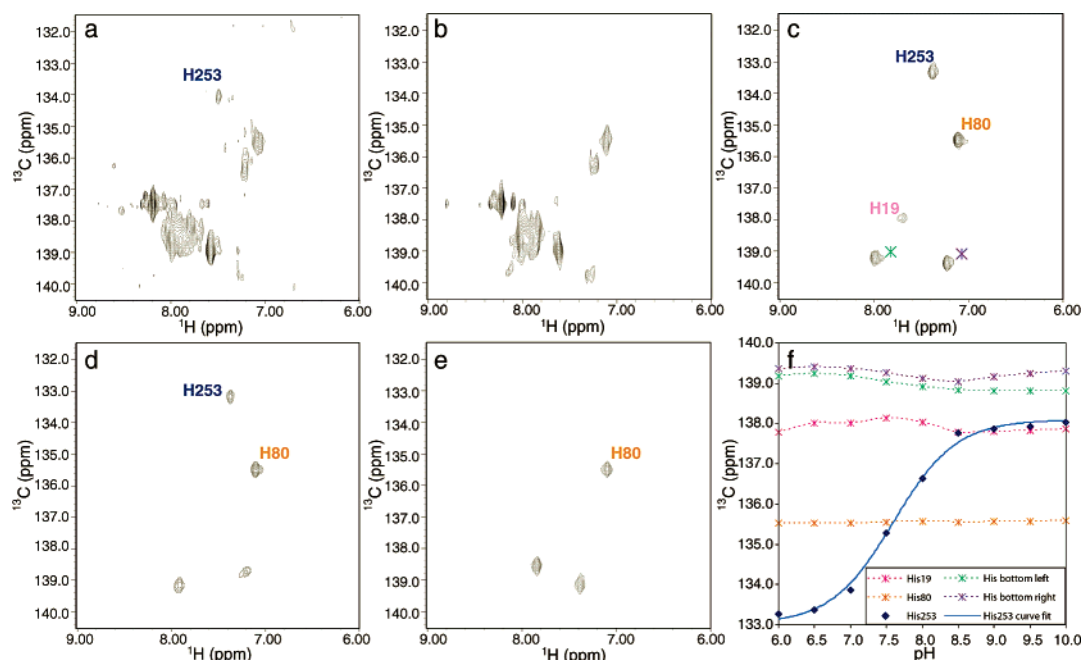
FIGURE 3: $^1H-^{13}C$ HSQC spectra of (a) AaLpxC, (b) AaLpxC-H253A, (c) AaLpxC-mut7, (d) AaLpxC-mut8, and (e) AaLpxC-mut9 with histidine residues selectively ^{13}C-labeled at the C2′-position. Resonances of H19, H80, and H253 are labeled. Zinc-binding histidines H74 and H226 are indicated with asterisks in panel c. (f) pH titration curve of H253 in AaLpxC-mut7.

activity (*24*). We expect the apparent pK_a values of these ionization states to correspond to the pK_a values of key catalytic residues, such as the general acid, the general base, or the residues that stabilize the transition state. To investigate whether H253 serves any of these roles in LpxC, we set out to determine the pK_a of H253 in free AaLpxC and to compare it with the pH-dependent ionizations measured by steady-state kinetics.

The 2D $^1H-^{13}C$ HSQC spectrum of wild-type AaLpxC allowed resolution of H253 from the remaining 10 histidines at pH 6.5 (Figure 3a). The C2′/H2′ resonance of H253 was assigned by comparing the spectrum of AaLpxC with that of AaLpxC-H253A (Figure 3a,b). Mutation of H253A caused the selective disappearance of the resonance assigned to H253, while resonances from all other histidines remained. On the basis of its chemical shift values and the titration curve obtained for H253 in AaLpxC-mut7 (Figure 3cf), we conclude that H253 is protonated at pH 6.5. Unfortunately, we were only able to follow the titration curve of H253 of the wild-type enzyme up to pH 8.5. At pH values above 8.5, the resonance of H253 is severely broadened and could not be detected. Since the exchange broadening is most severe close to the pK_a value of the histidine, we estimate the pK_a of H253 in free AaLpxC to be higher than 8.5, but less than 10.0. The resonance of the deprotonated H253 could not be identified unambiguously, presumably due to the spectral overlap between H253 and other histidines.

Design of the AaLpxC Mutant AaLpxC-mut7. To overcome the resonance overlap problems and to determine an accurate pK_a for H253, we decided to mutate all nonconserved histidines of AaLpxC except H80. Although H80 is not conserved within the LpxC family of proteins, its side chain forms two hydrogen bonds with the carbonyl group of I232 and the amide group of V242, which may be important to maintain the stability of AaLpxC. The codon for H275 was changed to a stop codon to remove the seven disordered C-terminal residues. In addition to these histidine mutations

(H29N, H50A, H55N, H58N, H188Y, and H275stop), C181 was mutated to alanine to prevent chemical shift perturbation caused by slow oxidation.

This seven-residue mutated form of AaLpxC (AaLpxC-mut7) retains the correct fold and displays a $^1H-^{15}N$ HSQC spectrum similar to that of the wild-type protein (data not shown). It is also fully active and displays a pH−rate profile similar to that of the wild-type protein (see the results below), indicating that the catalytic mechanism remains largely unchanged and that none of the mutated residues contribute significantly to catalysis.

Resonance Assignment and Titration of Histidines in AaLpxC-mut7. All five remaining histidines (H19, H74, H80, H226, and H253) in AaLpxC-mut7 are well separated in the $^1H-^{13}C$ HSQC spectrum (Figure 3c). Resonances of H253 and H19 can be identified easily by the absence of the corresponding resonances in the $^1H-^{13}C$ HSQC spectra of the AaLpxC mutants containing the additional mutations of H19N (Figure 3d) or H19N and H253N (Figure 3e). The remaining three resonances belong to H80 and the two zinc-binding residues H74 and H226 (Figure 3e). Resonances of these two zinc-binding histidines can be identified on the basis of their downfield ^{13}C chemical shifts. Addition of EDTA to the sample caused loss of zinc ion and selective perturbation of these two resonances, supporting their role as the zinc-binding histidines (data not shown). The remaining cross-peak is assigned to H80.

To determine the pK_a of H253, we collected a set of 2D $^1H-^{13}C$ HSQC spectra of AaLpxC-mut7 at 37 °C at pH 6.0, 6.5, 7.0, 7.5, 8.0, 8.5, 9.0, 9.5, and 10.0 in buffers containing 95% H_2O, 5% D_2O, 100 mM KCl, and either 20 mM phosphate (pH 6.0−8.0) or 20 mM CHES (pH 8.5−10.0). In solutions with pH values from 6.0 to 10.0, only H253 has a titratable pK_a within this range. The titration curves of H74, H226, and H80 are essentially flat, consistent with their roles as zinc-binding residues and a hydrogen-bonded structural residue, respectively (Figure 3f). Although the

Table 3: pH-Dependent Ionizations of AaLpxC and AaLpxC-mut7

param	value measured	AaLpxC	AaLpxC-mut7
k_{cat}/K_M	C^a (μM^{-1} s^{-1})	1.0 ± 0.3	1.3 ± 0.4
	pK_1	6.1 ± 0.2	7.1 ± 0.2
	pK_2	9.0 ± 0.4	8.8 ± 0.3
V_{max}	C^a (s^{-1})	4.0 ± 0.9	2.3 ± 0.5
	pK_1	6.0 ± 0.2	6.5 ± 0.2
	pK_2	8.9 ± 0.2	8.8 ± 0.3

^{a} C is the maximal pH-independent value calculated for k_{cat}/K_M or V_{max}.

chemical shifts of H19 do not change much over the entire titration range either, the resonance of H19 at pH 6.0 is significantly weaker than that at pH 6.5, suggesting that H19 has a pK_a slightly below 6.0. The ^{13}C chemical shifts of C2′ H253 at different pH values showed a typical sigmoidal curve (Figure 3f). Fitting these values to eq 1 yielded a pK_a of 7.6 $\pm$ 0.1 for H253.

pH Dependence of AaLpxC and AaLpxC-mut7 Activity at 37 °C. To compare the pK_a value of H253 determined in the current NMR study with the pH-dependent ionizations of LpxC catalysis, the pH−rate profiles of both wild-type AaLpxC and AaLpxC-mut7 were examined at 37 °C. The k_{cat}/K_M values are most relevant for comparison with the NMR titration of free enzyme as they describe the kinetic events between free enzyme and free substrate. To rule out perturbations related to substrate binding arising from the multiple histidine mutations in AaLpxC-mut7, we also obtained an estimate of the pH dependence of the k_{cat} profile by measuring the activity at saturating substrate concentrations.

As expected from the previous titrations at 50 °C (*24*), the pH dependencies of both V_{max} and k_{cat}/K_M are bell-shaped with similar inflection points for both proteins at 37 °C. For wild-type AaLpxC, the acidic limb of the profile exhibits a pK_1 of 6.1 $\pm$ 0.2 for k_{cat}/K_M or 6.0 $\pm$ 0.2 for V_{max}; the basic limb of the profile shows an ionization with a pK_2 of 9.0 $\pm$ 0.4 for k_{cat}/K_M or 8.9 $\pm$ 0.2 for V_{max} (Table 3 and Figure 4a). These pK_a values are in reasonable agreement with the previously determined pK_a values, although they do appear consistently higher (0.5−1.0 pH unit) in particular for pK_2. This difference probably arises from the temperature dependence of pK_a values belonging to ionizations of histidine, lysine, or zinc-bound water (*34−36*). The pH−rate profile of AaLpxC-mut7 is also bell-shaped with a pK_1 of 6.5 $\pm$ 0.2 for V_{max} or 7.1 $\pm$ 0.2 for k_{cat}/K_M, and a pK_2 of 9.0 $\pm$ 0.4 for V_{max} or 8.8 $\pm$ 0.3 for k_{cat}/K_M (Table 3 and Figure 4b). AaLpxC-mut7 retains essentially wild-type activity, suggesting that the catalytic machinery of LpxC remains intact in this mutant. Also, like wild-type AaLpxC, the V_{max} and k_{cat}/K_M profiles for AaLpxC-mut7 are nearly identical to each other, indicating that K_M remains pH-independent in this mutant and that the pH-dependent ionizations measured reflect key chemical steps of the reaction. The pK_2 values of 8.8 for k_{cat}/K_M or 9.0 for V_{max} in AaLpxC-mut7 are unchanged compared to the values reported for wild-type LpxC, demonstrating that the ionization entity associated with pK_2 of wild-type AaLpxC remains unperturbed in AaLpxC-mut7. The only observable difference between wild-type AaLpxC and the multihistidine mutant is the perturbation of pK_1 in AaLpxC-mut7 ($\sim$0.6 pH unit). Which of these

mutations affected the ionization of the residue responsible for pK_1 remains unknown.

Inhibition of LpxC Activity by Molecular Scaffolds from the Substrate. One major difference between TU-514 and the real LpxC substrate UDP-3-*O*-acyl-*N*-acetylglucosamine is the absence of the UDP moiety in TU-514. It is of considerable interest to speculate where the UDP moiety interacts with the protein and whether it contributes significantly to the binding energy. We had previously observed a hydrophobic pocket extending from the active site to the space between the two helices of domain I. It was hypothesized that this region might be accessible to the UDP moiety (*3*). In the refined solution structure, although such a hydrophobic pocket still exists, it is much more compact and is less likely to accommodate the bulky UDP group. An alternative model for UDP binding was recently proposed by Whittington et al. (*4*), suggesting that the space surrounded by insert II and α-helices of domain II may be interacting with the UDP group. To test this hypothesis, we have titrated UMP and UDP with AaLpxC and with the AaLpxC−TU-514 complex. Neither UMP nor UDP resulted in noticeable perturbation of any backbone NH resonances, suggesting that the interaction of the UDP moiety with the LpxC enzyme is weak, and may not contribute significantly to the binding energy (data not shown). Additionally, we have assayed AaLpxC activity in the presence of 2, 20, or 200 μM UMP or UDP. Inhibition of enzyme activity did not occur under any condition, indicating that, even at elevated concentrations, UMP or UDP alone is not sufficient to compete with the UDP-3-*O*-acyl-*N*-acetylglucosamine substrate for binding (data not shown).

Excluding the weak interaction between the UDP moiety and LpxC, the majority of the binding energy of the LpxC substrate would have to come from the encapsulation of the acyl chain of the substrate in the hydrophobic passage of LpxC or the interaction of the hexose ring in the active site. It has recently been reported that fatty acids with an acyl chain containing more than six carbon atoms bind LpxC with micromolar affinity (*4*). To investigate whether these fatty acids can serve as inhibitors of LpxC, we assayed the activity of both AaLpxC and EcLpxC in the presence of 2, 20, or 200 μM myristate (C14) or laurate (C12) at 30 °C. Both myristate and laurate were determined to be weak inhibitors of AaLpxC, while essentially no inhibition was observed for EcLpxC activity by these compounds (Figure 5).

DISCUSSION

Role of H253 in LpxC Catalysis. The pH-dependent activity of an enzyme is indicative of the requirement for specific protonation states of key entities during catalysis. The rate constant k_{cat} describes the rate-limiting events of the overall reaction, while k_{cat}/K_M describes the kinetic events between the free enzyme and free substrate, from substrate binding up to and including the first irreversible step. Since the substrate UDP-3-*O*-acyl-*N*-acetylglucosamine does not contain any groups that titrate between pH 4.0 and pH 10.0, the pK_1 and pK_2 values measured for the pH dependence of k_{cat}/K_M in LpxC can be associated with the pK_a values of specific residues in the free protein, including zinc-bound water. The majority of zinc-dependent amidases display bell-shaped pH dependence, with pK_1 corresponding to the pK_a
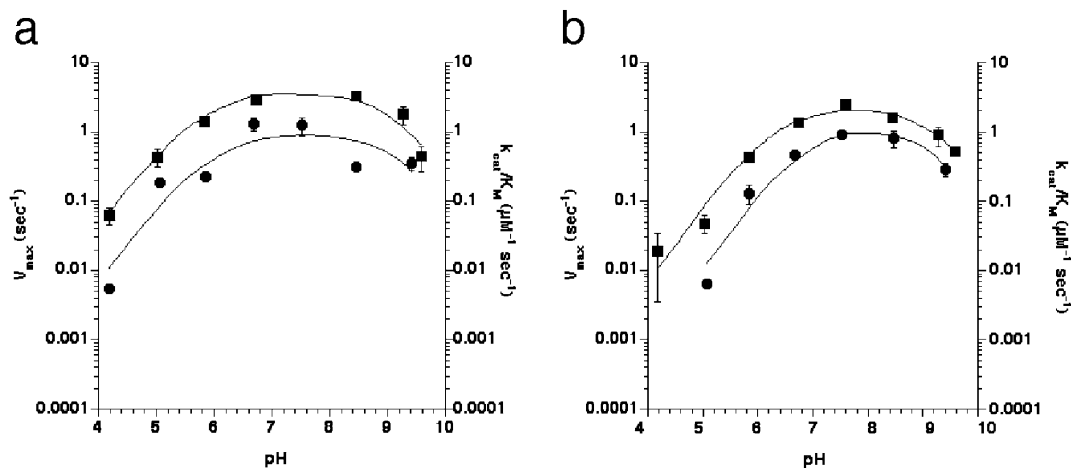
FIGURE 4: Bell-shaped pH dependence of V_{max} (squares) or k_{cat}/K_M (circles) for wild-type AaLpxC (a) and AaLpxC-mut7 (b).
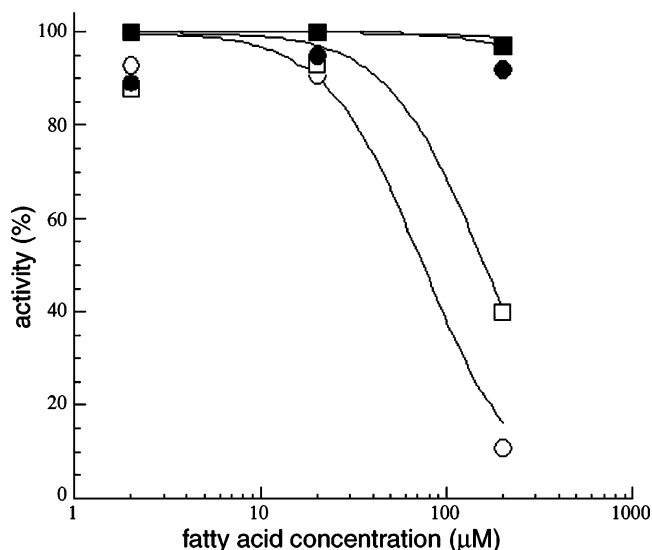
FIGURE 5: Inhibition of AaLpxC and EcLpxC by myristate and laurate in vitro. Percentage activities of the enzymes are normalized against wild-type LpxC's in the absence of fatty acids. Inhibition curves were fitted as the activity % = $100/(1 + [I]/IC_{50})$, where [I] stands for the inhibitor concentration. AaLpxC activity is weakly inhibited by myristate (open squares) or laurate (open circles), while essentially no inhibition is observed for EcLpxC by myristate (filled squares) or laurate (filled circles).

of a general base or zinc-bound water, and with pK_2 corresponding to the pK_a of a general acid or a residue that stabilizes the oxyanion intermediate. In the well-studied examples of carboxypeptidase A and thermolysin, the pK_1 residue is predicted to be a glutamate that must be deprotonated to serve as the general base and activate the zinc-bound water for nucleophilic attack (*37, 38*). The pK_2 residue is assigned as a histidine (H231) in thermolysin (*39*). Although the pK_2 residue has not been unequivocally assigned in carboxypeptidase A, it is speculated that an arginine (R127) stabilizes the oxyanion intermediate (*40*). In both cases, these residues must be protonated to stabilize the negative charge of the tetrahedral intermediate during catalysis. Recently, two models have been proposed for the mechanism of LpxC. It has been hypothesized that H253 could either act as the general base in LpxC catalysis (*3*) or stabilize the oxyanion intermediate through hydrogen bonding (*4*). Each of the proposed roles for H253 requires a different protonation state for this residue, suggesting that

the pK_a of H253 should be consistent with either pK_1 or pK_2 of the bell-shaped pH−rate profile, but not both.

The NMR titration of H253 in the wild-type enzyme showed that H253 is protonated at pH 6.5 and remains protonated up to pH 8.5. This result is consistent with the existence of a hydrogen bond between H253 and D234 as this type of interaction is known to elevate the pK_a of histidines (*41*). Since H253 is protonated at neutral pH and over the range of maximal enzyme activity, it can be excluded as the general-base residue that extracts a proton from the zinc-bound water. This conclusion is in agreement with a concurrent study that reports the identification of the general base as E73 (*24*). Though the pK_a of H253 could not be determined precisely in wild-type AaLpxC, it was estimated to fall between 8.5 and 10.0. Therefore, these data were not sufficient to eliminate H253 as a candidate for the pK_2 ionization, since its pK_a range is consistent with the pK_2 of 9.0 measured for the k_{cat}/K_M pH dependence of wild-type LpxC.

To investigate whether the pK_a of H253 corresponds to the pH-dependent pK_2 ionization of k_{cat}/K_M for LpxC, we mutated all nonconserved histidines (AaLpxC-mut7). Using this mutant, which retains full structural integrity, we could identify the resonance of the deprotonated H253 and determine its pK_a to be 7.6 ± 0.1 (Figure 3f). This mutant also retains high catalytic activity and possesses a pH−rate profile similar to that of the wild-type protein. Surprisingly, the value measured for the pK_a of H253 by NMR (7.6) in AaLpxC-mut7 is much lower (>1 unit) than the pK_2 value (8.8) measured for the enzymatic catalysis of this mutant, therefore eliminating H253 as being responsible for pK_2. The pK_a of H253 is also noticeably higher (0.5 unit) than the pK_1 of this mutant, further suggesting that H253 does not act as the catalytic base. This unexpected result is consistent with a concurrent study by McClerren et al. (*24*), showing that the pH dependence of the residual activity of the H253A mutant remains bell-shaped, with inflection points similar to those of the pH dependence of wild-type LpxC. Although the ionization of H253 is not reflected in the pH-dependent ionizations required for catalysis, the significant loss of activity in the H253A mutant (0.25% remaining activity) and its protonated form at neutral pH in wild-type AaLpxC suggests it might still be partially involved in the stabilization of the oxyanion intermediate.

Implications for the Design of Inhibitors. The availability of a highly refined solution structure allows us to identify three important areas surrounding the catalytic Zn^{2+} ion that may be important for the design of new LpxC inhibitors.

(I) Hydrophobic Passage. It is quite clear from the refined solution structure that the hydrophobic passage of insert II, formed by conserved residues I186, I189, L200, T203, V205, and Y212, must be important for the binding of the acyl chain of the substrate. This passage, located between the α-helix (αb′) and two β-strands (βa′ and βc′) of insert II, and partially surrounded by the loop connecting β1 and β2 of domain I, is quite narrow in AaLpxC, allowing insertion of only a linear acyl chain (Figure 1c). Consistent with this analysis, substrates lacking an acyl chain are extremely poor substrates for LpxC (*2*). In contrast, neither the NMR titrations nor the activity assays of AaLpxC in the presence of increasing concentrations of UMP or UDP showed any effects (data not shown), suggesting that the uridinyl phosphate portion of the substrate may not contribute to the substrate binding to a significant extent.

Interestingly, fatty acids alone were reported to bind AaLpxC with micromolar affinity (*4*). To test if these fatty acids could serve as inhibitors of LpxC, we have measured the in vitro activity of AaLpxC and EcLpxC in the presence of laurate and myristate. Both laurate and myristate inhibit AaLpxC weakly, but exhibit no inhibition against EcLpxC (Figure 5). These observations suggest that although inhibitors that mimic the acyl chain moiety of the substrate alone are not sufficient to inhibit catalysis with significant potency, the acyl chain interaction with the hydrophobic passage is likely to be an essential component in the design of potent LpxC inhibitors.

(II) Hydrophobic Patch. In the active site, on the opposite side of the α-helix (αb′) in insert II, there is a highly conserved hydrophobic patch consisting of F155, F180, and F182 (Figure 1c). This hydrophobic patch has been observed to interact partially with the hexose ring of TU-514 on the basis of the intermolecular NOEs (Figure 2a). Increasing its hydrophobicity, while maintaining the general shape of the molecule, may lead to increased binding affinity of the inhibitors.

(III) Basic Patch. In the active site, on the wall opposite the hydrophobic patch, a string of positively charge residues, including K227, R137, R250, and the ionized form of H253, form a contiguous basic surface (Figure 1c). Most likely, some of these residues, particularly R137 and R250, are involved in neutralizing the negative charge of the two phosphate groups of the UDP moiety in the LpxC substrate.

Significant effort has been devoted to the development of LpxC inhibitors that may serve as antibiotics for Gram-negative bacteria (*7, 13, 42−45*). These compounds can be roughly divided into three classes (Figure S2, Supporting Information). Most of the inhibitors in the first class are derivatives of L-161,240 (*42−44*). It is unclear whether these compounds bind in the hydrophobic passage or interact with the hydrophobic patch within the active site. Given the narrowness of the hydrophobic passage, some compounds with bulky chains may not be able to fit within this passage. The second class of compounds, including TU-514, are designed to mimic the natural substrate of LpxC and bind in the hydrophobic passage (*7, 13*). They do not contain a second hydrophobic moiety to interact with the hydrophobic

patch in the active site. However, their effectiveness against a large number of diverse LpxC orthologues suggests that the efficient interaction of inhibitors with the acyl chain passage of LpxC may be one of the most important features in the design of broad-spectrum inhibitors. Screening of a diverse compound library has identified a third class of potent inhibitors (BB-78484 and BB-78485) that contain a hydroxamate group but feature two branching aromatic moieties, suggesting that both the hydrophobic passage and the hydrophobic patch are being utilized (*45*).

On the basis of the above analysis, we propose that the best LpxC inhibitors should contain (1) a zinc-chelating group situated between two hydrophobic molecular moieties and (2) a negatively charged group or polar group capable of forming salt bridges or hydrogen bonds with the basic patch. For the hydrophobic fragment to fit within the hydrophobic passage, a linear chemical group without branches is preferable and the total length from the hydroxamate group (which presumably binds Zn^{2+}) to the terminal end of the linear fragment should be less than 15 Å. Any hydrophobic group with a length beyond 15 Å might require flexibility to fit the curved surface extending the hydrophobic passage, where the terminal methyl and the last two methylene groups of the TU-514 acyl chain are located.

ACKNOWLEDGMENT

SUPPORTING INFORMATION AVAILABLE

Figures showing the synthetic route of TU-514 from [$^{13}C_6$]-D-glucose and an illustration of three classes of LpxC inhibitors (PDF). This material is available free of charge via the Internet at http://pubs.acs.org.

REFERENCES

1. Raetz, C. R. H., and Whitfield, C. (2002) Lipopolysaccharide endotoxins, *Annu. Rev. Biochem. 71*, 635−700.
2. Jackman, J. E., Raetz, C. R. H., and Fierke, C. A. (1999) UDP-3-O-(R-3-hydroxymyristoyl)-N-acetylglucosamine deacetylase of Escherichia coli is a zinc metalloenzyme, *Biochemistry 38*, 1902−1911.
3. Coggins, B. E., Li, X., McClerren, A. L., Hindsgaul, O., Raetz, C. R. H., and Zhou, P. (2003) Structure of the LpxC deacetylase with a bound substrate-analog inhibitor, *Nat. Struct. Biol. 10*, 645−651.
4. Whittington, D. A., Rusche, K. M., Shin, H., Fierke, C. A., and Christianson, D. W. (2003) Crystal structure of LpxC, a zinc-dependent deacetylase essential for endotoxin biosynthesis, *Proc. Natl. Acad. Sci. U.S.A. 100*, 8146−8150.
5. Jackman, J. E., Raetz, C. R. H., and Fierke, C. A. (2001) Site-directed mutagenesis of the bacterial metalloamidase UDP-(3-O-acyl)-N-acetylglucosamine deacetylase (LpxC). Identification of the zinc binding site, *Biochemistry 40*, 514−523.
6. Onishi, H. R., Pelak, B. A., Gerckens, L. S., Silver, L. L., Kahan, F. M., Chen, M. H., Patchett, A. A., Galloway, S. M., Hyland, S. A., Anderson, M. S., and Raetz, C. R. H. (1996) Antibacterial agents that inhibit lipid A biosynthesis, *Science 274*, 980−982.
7. Jackman, J. E., Fierke, C. A., Tumey, L. N., Pirrung, M., Uchiyama, T., Tahir, S. H., Hindsgaul, O., and Raetz, C. R. H. (2000) Antibacterial agents that target lipid A biosynthesis in gram-negative bacteria. Inhibition of diverse UDP-3-O-(R-3-hydroxymyristoyl)-N-acetylglucosamine deacetylases by substrate analogs containing zinc binding motifs, *J. Biol. Chem. 275*, 11002−11009.

8. Clore, G. M., and Gronenborn, A. M. (1998) New methods of structure refinement for macromolecular structure determination by NMR, *Proc. Natl. Acad. Sci. U.S.A. 95*, 5891−5898.

9. Bax, A. (2003) Weak alignment offers new NMR opportunities to study protein structure and dynamics, *Protein Sci. 12*, 1−16.

10. Lipsitz, R. S., and Tjandra, N. (2004) Residual dipolar couplings in NMR structure analysis, *Annu. Rev. Biophys. Biomol. Struct. 33*, 387−413.

11. Prestegard, J. H., Bougault, C. M., and Kishore, A. I. (2004) Residual dipolar couplings in structure determination of biomolecules, *Chem. Rev. 104*, 3519−3540.

12. Whistler, R. L., Wolfrom, M. L., BeMiller, J. N., and Shafizadeh, F. (1963) *Methods in Carbohydrate Chemistry*, pp 409−410, Academic Press, New York.

13. Li, X., Uchiyama, T., Raetz, C. R. H., and Hindsgaul, O. (2003) Synthesis of a carbohydrate-derived hydroxamic acid inhibitor of the bacterial enzyme (LpxC) involved in lipid A biosynthesis, *Org. Lett. 5*, 539−541.

14. Yang, D., Venters, R. A., Mueller, G. A., Choy, W. Y., and Kay, L. E. (1999) TROSY-based HNCO pulse sequences for the measurement of ^1HN-^{15}N, ^{15}N-^{13}CO, ^1HN-^{13}CO, ^{13}CO-$^{13}C^\alpha$ and ^1HN-$^{13}C^\alpha$ dipolar couplings in ^{15}N, ^{13}C, ^2H-labeled proteins, *J. Biomol. NMR 14*, 333−343.

15. Ottiger, M., Delaglio, F., and Bax, A. (1998) Measurement of J and dipolar couplings from simplified two-dimensional NMR spectra, *J. Magn. Reson. 131*, 373−378.

16. Delaglio, F., Grzesiek, S., Vuister, G. W., Zhu, G., Pfeifer, J., and Bax, A. (1995) NMRPipe: a multidimensional spectral processing system based on UNIX pipes, *J. Biomol. NMR 6*, 277−293.

17. Bartels, C., Xia, T., Billeter, M., Güntert, P., and Wüthrich, K. (1995) The program XEASY for computer-supported NMR spectral analysis of biological macromolecules, *J. Biol. NMR 6*, 1−10.

18. Garrett, D. S., Powers, R., Gronenborn, A. M., and Clore, G. M. (1991) A common sense approach to peak picking in two-, three-, and four-domensional spectra using automatic computer analysis of contour diagrams, *J. Magn. Reson. 95*, 214−220.

19. Clore, G. M., Gronenborn, A. M., and Bax, A. (1998) A robust method for determining the magnitude of the fully asymmetric alignment tensor of oriented macromolecules in the absence of structural information, *J. Magn. Reson. 133*, 216−221.

20. Dosset, P., Hus, J. C., Marion, D., and Blackledge, M. (2001) A novel interactive tool for rigid-body modeling of multi-domain macromolecules using residual dipolar couplings, *J. Biomol. NMR 20*, 223−231.

21. Schwieters, C. D., Kuszewski, J. J., Tjandra, N., and Clore, G. M. (2003) The Xplor-NIH NMR molecular structure determination package, *J. Magn. Reson. 160*, 65−73.

22. Okar, D. A., Felicia, N. D., Gui, L., and Lange, A. J. (1997) Labeling of recombinant protein for NMR spectroscopy: global and specific labeling of the rat liver fructose 2,6-bisphosphatase domain, *Protein Expression Purif. 11*, 79−85.

23. Markley, J. L., Bax, A., Arata, Y., Hilbers, C. W., Kaptein, R., Sykes, B. D., Wright, P. E., and Wüthrich, K. (1998) Recommendations for the presentation of NMR structures of proteins and nucleic acids, *Pure Appl. Chem. 70*, 117−142.

24. McClerren, A. L., Zhou, P., Guan, Z., Raetz, C. R. H., and Rudolph, J. (2004) Kinetic analysis of the zinc-dependent deacetylase in the lipid A biosynthetic pathway, *Biochemistry 43*, 1106−1113.

25. Fersht, A. (1999) *Structure and Mechanism in Protein Science: A Guide to Enzyme Catalysis and Protein Folding*, W. H. Freeman and Co., New York.

26. Cleland, W. W. (1979) Statistical analysis of enzyme kinetic data, *Methods Enzymol. 63*, 103−138.

27. Breeze, A. L. (2000) Isotope-filtered NMR methods for the study of biomolecular structure and interactions, *Prog. Nucl. Magn. Reson. Spectrosc. 36*, 323−372.

28. Walters, K. J., Ferentz, A. E., Hare, B. J., Hidalgo, P., Jasanoff, A., Matsuo, H., and Wagner, G. (2001) Characterizing protein-protein complexes and oligomers by nuclear magnetic resonance spectroscopy, *Methods Enzymol. 339*, 238−258.

29. Zwahlen, C., Legault, P., Vincent, S. J. F., Greenblatt, J., Konrat, R., and Kay, L. E. (1997) Methods for Measurement of Intermo-

lecular NOEs by Multinuclear NMR Spectroscopy: Application to a Bacteriophage N-Peptide/boxB RNA Complex, *J. Am. Chem. Soc. 119*, 6711−6721.

30. Walters, K. J., Matsuo, H., and Wagner, G. (1997) A Simple Method to Distinguish Intermonomer Nuclear Overhauser Effects in Homodimeric Proteins with C2 Symmetry, *J. Am. Chem. Soc. 119*, 5958−5959.

31. Walters, K. J., Dayie, K. T., Reece, R. J., Ptashne, M., and Wagner, G. (1997) Structure and mobility of the PUT3 dimer, *Nat. Struct. Biol. 4*, 744−750.

32. Zhou, P., Sun, L. J., Dötsch, V., Wagner, G., and Verdine, G. L. (1998) Solution structure of the core NFATC1/DNA complex, *Cell 92*, 687−696.

33. Ferentz, A. E., Opperman, T., Walker, G. C., and Wagner, G. (1997) Dimerization of the UmuD' protein in solution and its implications for regulation of SOS mutagenesis, *Nat. Struct. Biol. 4*, 979−983.

34. Woolley, P. (1975) Models for metal ion function in carbonic anhydrase, *Nature 258*, 677−682.

35. Kunugi, S., Hirohara, H., and Ise, N. (1982) pH and temperature dependences of thermolysin catalysis. Catalytic role of zinc-coordinated water, *Eur. J. Biochem. 124*, 157−163.

36. Izatt, R. M., and Christensen, J. J. (1976) *Heats of proton ionization, pK, and related thermodynamic quantities*, 3rd ed., Vol. 1, CRC Press, Cleveland, OH.

37. Christianson, D. W., and Lipscomb, W. N. (1989) Carboxypeptidase A, *Acc. Chem. Res. 22*, 62−69.

38. Matthews, B. W. (1988) Structural basis of the action of thermolysin and related zinc peptidases, *Acc. Chem. Res. 21*, 333−340.

39. Beaumont, A., O'Donohue, M. J., Paredes, N., Rousselet, N., Assicot, M., Bohuon, C., Fournie-Zaluski, M. C., and Roques, B. P. (1995) The role of histidine 231 in thermolysin-like enzymes. A site-directed mutagenesis study, *J. Biol. Chem. 270*, 16803−16808.

40. Phillips, M. A., Fletterick, R., and Rutter, W. J. (1990) Arginine 127 stabilizes the transition state in carboxypeptidase, *J. Biol. Chem. 265*, 20692−20698.

41. Harris, T. K., and Turner, G. J. (2002) Structural basis of perturbed pKa values of catalytic groups in enzyme active sites, *IUBMB Life 53*, 85−98.

42. Pirrung, M. C., Tumey, L. N., McClerren, A. L., and Raetz, C. R. H. (2003) High-throughput catch-and-release synthesis of oxazoline hydroxamates. Structure-activity relationships in novel inhibitors of Escherichia coli LpxC: in vitro enzyme inhibition and antibacterial properties, *J. Am. Chem. Soc. 125*, 1575−1586.

43. Pirrung, M. C., Tumey, L. N., Raetz, C. R. H., Jackman, J. E., Snehalatha, K., McClerren, A. L., Fierke, C. A., Gantt, S. L., and Rusche, K. M. (2002) Inhibition of the antibacterial target UDP-(3-O-acyl)-N-acetylglucosamine deacetylase (LpxC): isoxazoline zinc amidase inhibitors bearing diverse metal binding groups, *J. Med. Chem. 45*, 4359−4370.

44. Kline, T., Andersen, N. H., Harwood, E. A., Bowman, J., Malanda, A., Endsley, S., Erwin, A. L., Doyle, M., Fong, S., Harris, A. L., Mendelsohn, B., Mdluli, K., Raetz, C. R. H., Stover, C. K., Witte, P. R., Yabannavar, A., and Zhu, S. (2002) Potent, novel in vitro inhibitors of the *Pseudomonas aeruginosa* deacetylase LpxC, *J. Med. Chem. 45*, 3112−3129.

45. Clements, J. M., Coignard, F., Johnson, I., Chandler, S., Palan, S., Waller, A., Wijkmans, J., and Hunter, M. G. (2002) Antibacterial Activities and Characterization of Novel Inhibitors of LpxC, *Antimicrob. Agents Chemother. 46*, 1793−1799.

46. Cornilescu, G., Delaglio, F., and Bax, A. (1999) Protein backbone angle restraints from searching a database for chemical shift and sequence homology, *J. Biomol. NMR 13*, 289−302.

47. Güntert, P., Mumenthaler, C., and Wüthrich, K. (1997) Torsion angle dynamics for NMR structure calculation with the new program DYANA, *J. Mol. Biol. 273*, 283−298.

48. Clore, G. M., and Garrett, D. S. (1999) R-factor, Free R, and complete cross-validation for dipolar coupling refinement of NMR structures, *J. Am. Chem. Soc. 121*, 9008−9012.

49. Davis, I. W., Murray, L. W., Richardson, J. S., and Richardson, D. C. (2004) MOLPROBITY: structure validation and all-atom contact analysis for nucleic acids and their complexes, *Nucleic Acids Res. 32*, W615−W619.

50. Lovell, S. C., Davis, I. W., Arendall, W. B., 3rd, de Bakker, P. I., Word, J. M., Prisant, M. G., Richardson, J. S., and Richardson,

D. C. (2003) Structure validation by Cα geometry: ϕ,ψ and Cβ deviation, *Proteins 50*, 437−450.

51. Petrey, D., and Honig, B. (2003) GRASP2: visualization, surface properties, and electrostatics of macromolecular structures and sequences, *Methods Enzymol. 374*, 492−509.

52. Koradi, R., Billeter, M., and Wüthrich, K. (1996) MOLMOL: a program for display and analysis of macromolecular structures, *J. Mol. Graphics 14*, 51−55.